ACS OMEGA

http://pubs.acs.org/journal/acsodf

Article

Deciphering the Kinetic Study of Sodium Dodecyl Sulfate on Ag Nanoparticle Synthesis Using *Cassia siamea* Flower Extract as a Reducing Agent

Sajjad Hussain Parrey, Mohsin Maseet, Rabia Ahmad, and Abbul Bashar Khan*

Cite This: *ACS Omega* 2021, 6, 12155−12167

Read Online

ACCESS | Metrics & More | Article Recommendations | Supporting Information

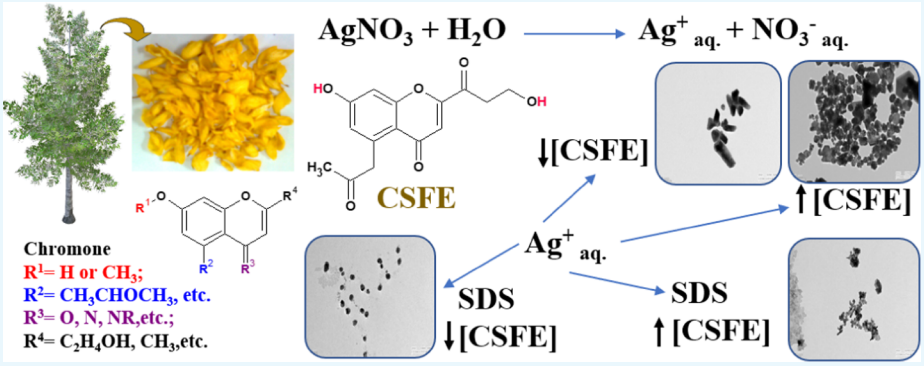

ABSTRACT: Silver nanoparticles (Ag NPs) were synthesized using *Cassia siamea* flower petal extract (CSFE) as a reducing agent for the first time. In its presence and absence, the correlative effects of the anionic surface-active agent sodium dodecyl sulfate (SDS) were studied with respect to the development and texture of Ag NPs. Under different reagent compositions, the Ag NPs were inferred by localized surface plasmon resonance peaks between 419 and 455 nm. In the absence of SDS, there was a small eminence at 290 and around 350 nm, pointing toward the possibility of irregular polytope Ag NPs, which was confirmed in the transmission electron microscopy images. This elevation vanished beyond the cmc of [SDS], resulting in spherical and oval shaped Ag NPs. The effects of reagent concentrations were studied at 25 °C and around 7 and 9 pH in the absence and presence of SDS, respectively. Also, kinetic studies were performed by UV−visible spectrophotometry. Prodigious effects on shape and size were found under different synthesis conditions in terms of hexagonal, rod-, irregular-, and spherical shaped Ag NPs. Furthermore, the antimycotic activity of the synthesized Ag NPs was established on different *Candida* strains, and best results were found pertaining *Candida tropicalis*. The ensuing study impels the control of texture and dispersity for Ag NPs by CSFE and SDS, and the resultant polytope Ag NPs could be a future solution for drug-resistant pathogenic fungi.

1. INTRODUCTION

Nobel metal nanoparticle synthesis has been studied through different methodologies from the last few decades.[1] Physicists, chemists, and biologists have been equally fascinated by these nanoparticles due to their high potential values concerning optics, catalysis, biomedicine, environmental remediations, and so forth.[2−4] Biomimetic route has been a cheap, easy, and environmentally friendly way of preparing nanomaterials.[5] The texture and size of nanoparticles have been impacted remarkably due to the natural organic compounds present in the plant extracts.[6] Although researchers have succeeded in controlling the textural aspects of metal nanoparticles via chemical reduction and physical methods with the variations in pH, concentration, chemical stabilizer, temperature, and irradiation,[6−9] research on green methodologies needs to be done in order to understand the development of metal NPs, through which control over the shape and size of nanoparticles while synthesizing them through biogenic methods could be enhanced.[10] *Cassia siamea,* also known as *Senna siamea*, is an evergreen tree that blossoms with yellow flowers in the late autumn and spring seasons in Asian countries.[11] Its different parts have been utilized by people in various ways, both medicinally and in daily life in Asia.[12] Its leaves are used as vegetables by the natives of Thailand.[13]

One of the paramount steps in the synthesis of nanoparticles has been the initial stage of nucleation.[14] From the literature, it was observed that the textural features of nanoparticles were

Received: February 16, 2021
Accepted: April 15, 2021
Published: April 28, 2021

dependent on early stages of nanoparticle formation, particularly the nucleation stage.[15,16] Henglein proposed the advantages of smaller colloidal particles due to easy monitoring by UV−visible spectrometry.[17] Although literature contains interaction studies of SDS and silver nanoparticles (Ag NPs) through both chemical reduction and biomimetic methods,[18,19] the present study aims at studying the effects of SDS on the overall formation of Ag NPs through a biomimetic method using *C. siamea* flower extract.

Ag NPs have been known for their promising antibacterial and antifungal properties.[20] Many studies have highlighted the effectiveness of Ag NPs toward microbes such as *Escherichia coli, Staphylococcus aureus, Bacillus subtilis, Candida albicans,* and *Trichosporon asahii*.[21,22] Recently, Aisidi et al. reported the antibacterial activity of green-synthesized Ag NPs against *S. aureus* and *Coliform*.[23] Rodríguez-Torres et al. reported the cooperative antifungal assay of spherical Ag NPs with *Artemisia absinthium* toward few *Candida* sp.[24] It has been found that they bind to a wide range of targets in proteins which made them as potential non-resistant antimicrobial agents.[25] However, the effectiveness of Ag NPs as antimicrobial agents have been found dependent on shape, size, and uniformity of nanoparticles, as it does in a plethora of other applications such as catalysis, optics, and electronic applications.[26,27] Even in the earliest applications of silver and gold as medicines, size and dispersal aspects were of considerable interest.[28] Lately, antimycotic studies have been reported mostly for spherical Ag NPs;[29,30] herein, the studies have been performed with polytope hexagonal Ag NPs. The Ag NPs were tested for antimycotic efficacy against *Candida* sp., and encouraging results were obtained in terms of inhibition of growth and fungicidal activity.

Concerning the synthesis of Ag NPs from the recent literature, it was found that most studies have been performed using leaf extracts.[12,13,31] Only a few were pertained to flower extracts.[32] The effects of various surfactants on the shape and size of Ag NPs have been studied using both plant and chemical reducing agents.[33,34] However, regarding plant extract-mediated synthesis, mostly cationic surfactants have been used. Zaheer et al. reported the ionic surfactant effect on green-synthesized Ag NPs using *Mentha* leave extract.[35] Khan et al. synthesized Ag NPs in the presence of CTAB using *Raphanus sativus* extract.[36] Although various studies have been reported using plant extracts and surfactants, most of the times their individual effects have been reported.[33,35,37] Therefore, while using flower extract as a reducing agent, it was imperative to study the effect of anionic surfactants on the formation and structural features of Ag NPs.[38] Hitherto, a relationship is developed between the effects of the anionic surfactant [SDS] and *Cassia siamea* flower petal extract ([CSFE]) by studying their mutual effects on the synthesis and overall texture development of Ag NPs. Sodium dodecyl sulfate (SDS) was considered as an anionic surfactant with the formula of $C_{12}H_{25}NaSO_4$. SDS has been studied in various aspects of surface and colloid chemistry.[39,40] Subsequently, the nucleation stage of Ag NP synthesis got elongated, particularly beyond the cmc value of [SDS] considered. Also, complementary shapes were observed with the variation of [CSFE] and [SDS] with respect to each other. The kinetics was performed by following the Esumi model, and the mechanism was proposed based on Watzky, Turkevich, and Henglein findings.[9,41]

2. EXPERIMENTAL SECTION

2.1. Choice of Materials and Synthesis. Silver nitrate ($AgNO_3$) is a stable, easily water-soluble, and direct weighing Ag salt. Solutions obtained from it have been found to be stable for >100 h[42] Since being listed by U.S.-E.P.A as a green chemical, SDS has been of less concern to human health and environment.[43] *C. siamea*, an evergreen flowering plant, has been known for its medicinal and vegetable value particularly in Southeast Asia.[13] Being a biannual flowering plant, it was a convenient source of green reducing agents over an extended period. $AgNO_3$ and SDS ($C_{12}H_{25}SO_4Na$) were procured from Merck-India and Fisher & Co., respectively. SDS was further purified and recrystallized in ethanol−water combination. Stable solutions of $AgNO_3$ and SDS were prepared by direct weighing and stored in brown bottles.

2.1.1. Preparation of CSFE. The flower petals were collected directly from *C. siamea* trees near the Department of Nanotechnology in Jamia Millia Islamia. The bright yellow-colored petals were separated and shade-dried. In order to remove the dust particles, the collected flower petals were gently caressed in sequence, rinsed in double-distilled water (DDW), and then thoroughly washed in DDW. The petals were first dried in air and then in an oven at 45 °C for 2 h. After that, they were stored in airtight jars for further use in the synthesis of Ag NPs.

CSFE was prepared by adding 200 mg of dry flower petal powder (1 petal = 4 mg) in 100 cm^3 of DDW. It was stirred in a 250 mL Erlenmeyer flask at 60 °C in a water bath for 30 min. The light-colored solution was refrigerated at 4 °C. It was then filtered by Whatman filter paper no. 42 and stored in a brown bottle in a refrigerator. A new extract was prepared, if the already prepared extract exceeded 24 h.

2.1.2. Synthesis of Ag NPs. In a one-pot synthesis, required concentrations of silver nitrate ($AgNO_3$) were added in DDW and the Ag^+ ions in it were reduced by using CSFE. The precise amount of CSFE for the synthesis of Ag NPs was decided by UV−visible spectrometry. Reagents were temperature-maintained prior to the reaction. The solutions of $AgNO_3$ (aq), SDS, and CSFE were mixed in different ratios to observe and study the concentration effects on surface plasmon resonance (SPR), shape, size, distribution, kinetics, stability, and structure of Ag NPs (Table S1).

The emergence of Ag NPs and the effects of concentrations were monitored by UV−visible spectrometry (Figure S2). Kinetically, the synthesis of Ag NPs was monitored for 120 min mostly (Figure S3). The kinetics of concerned five (I−V) sets in the synthesis of Ag NPs, comprising nucleation, growth, and aggregation, was graphically plotted by measuring the absorbance at SPR (λ_{max}) and λ_{CSFE} as a function of time (Figure S8). Also, the temperature effect on the synthesis in the presence and absence of SDS at SPR was carried at 20, 25, and 30 °C (Figure S6k,l). The reaction was executed in a temperature-controlled water bath in a three-necked flask. The samples were pipetted out at required time intervals for absorption monitoring. The reaction mixture turned faint colorful within the first 15−25 min. The spectra were obtained between 220 and 700 nm for the synthesis of Ag NPs. The kinetic analysis under different reaction conditions was performed by measuring the absorption at SPR and absorption of CSFE as a function of time. For different conditions, UV−visible spectrometry showed a broad peak with λ_{max} between 419 and 455 nm, confirming the SPR value for Ag NPs (Figure

https://doi.org/10.1021/acsomega.1c00847
ACS Omega 2021, 6, 12155−12167

S3). Depending on [$AgNO_3$], [CSFE], and [SDS], it changed from colorless to a light yellowish, reddish, or brown coloured solution. In the absence of SDS and at higher [$AgNO_3$] and [CSFE], the solutions became dark (generally brown) in color due to the large size and aggregation of Ag NPs, as the reaction time reached toward 120 min, while the lower [$AgNO_3$] reaction mixtures attain a translucent yellow or reddish color but did not became dark (Figure S1). The pH of the starting reaction mixtures in the absence of SDS was noticed between 6.8 and 7.2, while in the presence of SDS, it was found around 9.5. After the completion of the reaction, it was noticed to fall toward 6.2 and 8.4 in the absence and presence of SDS, respectively. As it has been recommended not to utilize buffer solutions in surfactants, pH was not maintained during the synthesis.[44,45]

In order to collect the Ag NPs, the solutions were centrifuged at 10,000 rpm for 20 min per aliquot. The pellets obtained were redispersed in DDW and again centrifuged, oven-dried, and used for characterization. FTIR analysis was performed primarily for establishing the reducing characteristic of CSFE by noticing the intensity changes in various CSFE extract peaks.[38]

2.2. Characterization. UV−visible spectrometry was performed on a Hitachi U 3900, having a resolution of 0.5 nm and a slit width of 2 nm, with solutions added in a 3 mL cuvette. The samples were scanned between 220 and 700 nm at steady time intervals and SPR (λ_{max}) versus time was executed to monitor the stages of CSFE-mediated Ag NP synthesis. FTIR analysis of CSFE and Ag NP solutions was carried out using a Tensor-37 instrument with a resolution of 0.6 cm^{-1} on the ATR mode. Cells from liquid samples were analyzed from 400 to 4000 cm^{-1}. pH inspection of the samples was done using an Eutech pH-510 appliance at 25 °C. A Lab India Pico$^+$ digital conductivity meter having a range of 10^{-3} to 200 mS, a resolution of 10^{-3}, and operating at 50 Hz frequency was used for conductivity study. KCl (0.1 N) was used for calibration with a cell constant of 1 cm^{-1}. Measurements were taken from capped 20 cm^3 cells immersed in a Julabo-MD electronic thermostatic water bath. Zeta potential values were obtained using a Malvern Nano ZS for [Ag^+ ion] of 0.0005 to 0.002 M in the reaction mixture. CSFE (5 and 10%) and 11 mM SDS were other reagent compositions used. RinA, Spectro scatter 201, was used for performing dynamic light scattering (DLS) measurements. Sample readings were recorded after four cycles in a 3 cm^3 cuvette at 25 °C at 90° scattering angle. The textural aspects related to synthesized Ag NPs were studied by using a transmission electron microscope, FEI Tecnai S Twin 200 kV. It was operated at 200 kV voltage and consisted of a 35 mm photography system with a magnification of 1,030,000×. Fresh samples were globule-coated on carbon−copper (Cu) grids, adroitly dried, and desiccated for imaging and selected area electron diffraction (SAED) pattern. X-ray diffraction (XRD) measurements between 20 and 80° were performed from a Rigaku Ultima-IV X-ray diffractometer, having Cu as a target and scintillation counter as a detector. It was operated at a voltage of 40 kV and a current of 44 mA. Dried granulated samples were impinged by X-rays from Cu Kα source with a wavelength (λ) of 0.15 nm.

2.3. Antifungal Assay. The synthesized Ag NPs in the absence of SDS were put through antimycotic assays. The testing was divided into two parts of determination of minimum inhibitory concentration (MIC) and growth curve study (GCS).

MIC data were determined by measuring the optical density at 600 nm (OD_{600}) in a microplate reader as per CSLI guidelines. For analyzing the growth curve, the OD_{595} of the cells was measured at 2 h intervals up to the stationary phase.

2.3.1. Antifungal Sensitivity Susceptibility Tests or MIC. *C. albicans* strain was grown for 24 h in the yeast extract peptone dextrose (YEPD) broth. Five microliters of four dilutions (5×10^3 to 5×10^6) were prepared from an overnight grown culture. These dilutions were spotted onto YEPD agar plates containing desired concentration of drugs and incubated for 48 h at 30 °C. MIC_{90} (minimum inhibitory concentration—90%) was determined by broth microdilution methods described in Clinical and Laboratory Standards Institute (CSLI) guidelines. MIC_{90} is termed as the concentration of drug that inhibits 90% growth of the organism in comparison to the controls containing no drug. The cell suspension containing 10^4 cells per mL^{-1} was added to the wells of 96-well microtiter plates containing serially diluted drug concentrations in equal amounts of media. The plates were incubated at 37 °C for 48 h. The results were determined by measuring OD_{600} in a microplate reader. The minimum concentration required for no colony growth under stipulated conditions, called as minimum fungicidal concentration (MFC), was determined after a 48 h incubation.

2.3.2. Growth Curve Study. Inoculum was obtained from the *Candida* primary culture, streaked on YEPD agar media, and incubated at 30 °C for 24 h. Colonies were obtained from the overnight incubated agar plates and inoculated into fresh YEPD media (50 mL) containing zero, IC_{90}, and $IC_{90}/2$ concentrations of Ag NPs. The cells were then incubated at 30 °C at 150 rpm. For analyzing the growth curve, the optical density (OD) of the cells was measured at 595 nm at intervals of 2 h up to the stationary phase. A graph was plotted between absorbance (A) and time (T) to study the growth curve pattern.

3. RESULTS AND DISCUSSION

3.1. Formation of Ag NPs. The preliminary corollary regarding the formation of metal NPs has been the specific SPR (λ_{max}) peak values, whose location has been found to be dependent on the size and morphology of nanoparticles.[17] Various factors have been found to govern the SPR values of the metal NPs, which include concentration of reagents and stabilizers, interaction time, aging of reagents, pH, duration of mixing, and temperature.[46] The SPR range for Ag NPs has been delineated between 385 and 530 nm.[47] In the present studies, the SPR became noticeable in 10−15 min. The λ_{max} peak increased in intensity and the crest attained a constant value after nearly 1 h of reaction.

At 25 °C, under the different concentrations of reagents, the synthesis of Ag NPs was comprehended with the occurrence of SPR in the UV−visible spectra between 419 and 455 nm (given in the Supporting Information, Figure S3). The SPR lies on the lower side of the UV−visible spectrum when the synthesis was carried at lower [$AgNO_3$] and beyond cmc [SDS]. The SPR values and the color variation of the formed Ag NPs solution were found to comply each other with yellow for small sized NPs, more toward 10 nm size, and brown for large sized, toward 100 nm size, NPs (Figure S1).

Both UV−visible (Figure S2) and FTIR (Figure 1) techniques established the usage of CSFE as a reducing agent in the synthesis process. From the individual UV−visible spectra of the reagents, the absorption around 250−260 nm

https://doi.org/10.1021/acsomega.1c00847
ACS Omega 2021, 6, 12155−12167

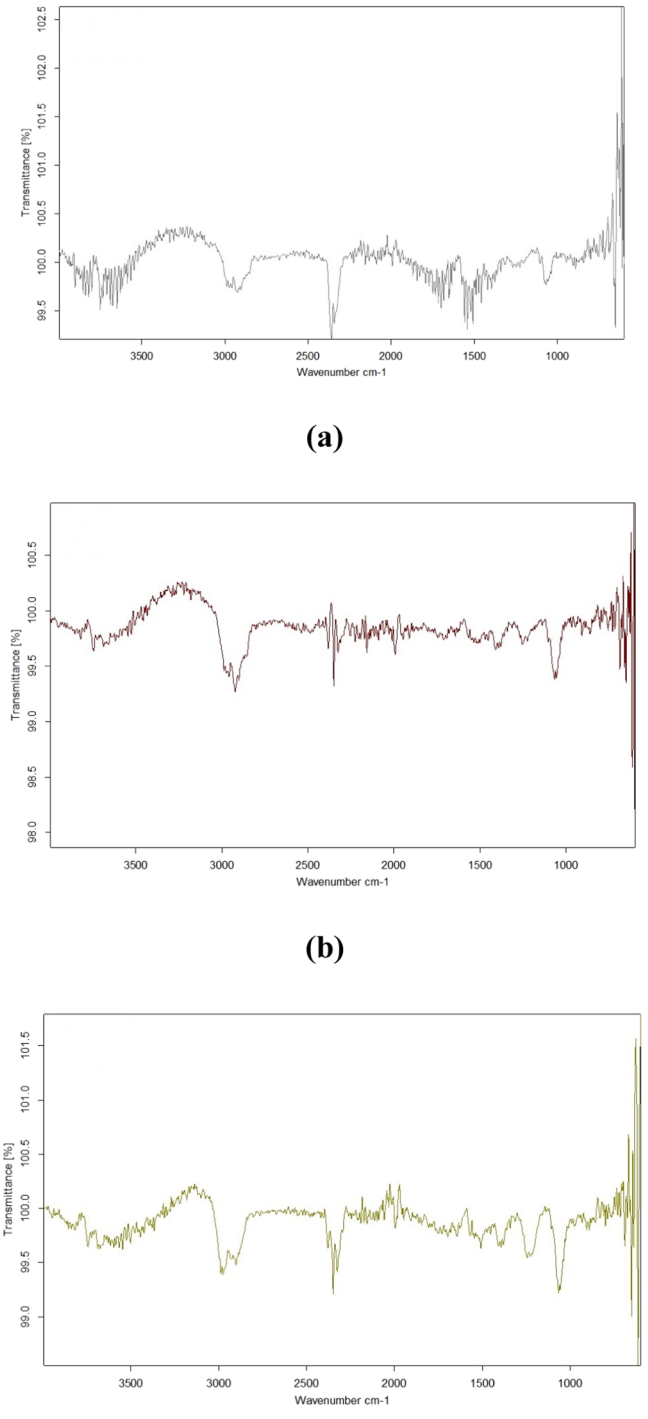

Figure 1. FTIR of (a) CSFE, (b) Ag NP solution in the absence of SDS, and (c) Ag NP solution in the presence of SDS.

was found to be that of CSFE. The λ_{CSFE} peak intensity decreased with the progress of reaction and with the increase in [Ag NPs].[48] As reported in Table S1, the synthesis was carried out in sets I–V. In the presence and absence of SDS, respectively, sets I and II were considered for the variation of [$AgNO_3$] (Figure S3a–f) and sets III and IV for the change in [CSFE] (Figure S3g–l). In set V, the [SDS] effect was studied with [$AgNO_3$] and [CSFE] being kept constant (Figure S3m–o). Except for set II, the UV–visible absorbance of CSFE exhibited a blue shift under different reagent concentrations (Figure S3).

In accordance with the UV–visible data concerning the usage of CSFE as the reducing agent and to ascertain the functional groups involved in the reduction of Ag^+ ions by CSFE, FTIR analysis was very useful. Regarding the FTIR spectra of CSFE and Ag NP solutions, many peak intensity variations were found between 400 and 4000 cm^{-1} (Figure 1a). However, the major change in intensity was conspicuous from 1100 to 2500 cm^{-1} at 1500, 1700, and 2400 cm^{-1}, which were found to be related to major functional groups of organic chemistry.[6,23] Evidently around 1500 cm^{-1}, there was a remarkable decrease in the intensity of the peaks which might be mainly related to the carbonyl (>C═O) part of various functional groups (Figure 1b,c). This group has been reported immensely in the reduction process for Ag NPs while using plant extracts.[6,20] Also, around 1630 cm^{-1}, there was a diminution which could be connected to vibrations of –NH bending and conjugated C═C stretching.[49] It has been copiously reported that the precursor salt ion reduction for the nanoparticle synthesis has been involved by the oxidation of carbonyl (>C═O) and organonitrogen compounds, which includes aldehydes, ketones, carboxylic acids, ethers, and esters and amines and amides.[6] From the various intensity variations in the FTIR spectra of the synthesized samples of Ag NPs in both the absence and presence of SDS, it was implied that the reduction of Ag^+ ions has been done by CSFE (Figure 1b,c). The characteristic organic functional groups that are believed to be involved in the reduction of Ag^+ ions could be mentioned with their FTIR absorptions as O–H stretching of alcohol and phenol (3285 cm^{-1}), alkane C–OH stretching (2926 cm^{-1}), carboxyl C═O bending (1880 cm^{-1}), C–N stretching of aliphatic amines (1052 cm^{-1}), aromatic C–H stretching (1627 cm^{-1}), C═O stretching of aldehydes (1687 cm^{-1}), polyphenol C–N stretching (1065 cm^{-1}), C–H bending of alkanes (1390 cm^{-1}), and C–H of alkanes (670 cm^{-1}).[20] This led to the outcome that the Ag^+ ions were effected to Ag NPs by CSFE. It was inferred that biomolecules such as *β*-sitosterol, chrysophanol, physcion, cassiamin (A-E), and cassiachromones present in *C. siamea* flower extract were involved in the formation of Ag NPs (Scheme 1).[50,51] The chromones have been most investigated among these compounds recently, and from the kinetic point of view, it was chosen as a model compound for reduction of Ag^+ ions to form a proposed mechanism (Scheme S1). The major changes were observed in the UV–visible absorption of CSFE at 264, 261, and 252 nm and λ_{SPR} at 421, 425, and 450 nm up to the first 15–20 min, when the [$AgNO_3$] was altered in the absence of SDS (Figure S3a–c), which indicated the nucleation stage, thereafter leading to growth phase, which may be ultimately the reason for the formation of nanorods and hexagonal shapes.[5]

Scheme 1. Synthesis of Ag NPs Using CSFE

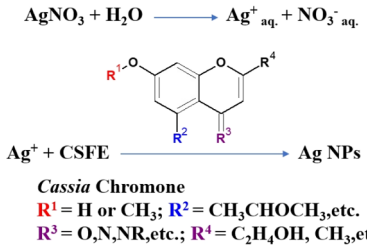

https://doi.org/10.1021/acsomega.1c00847
ACS Omega 2021, 6, 12155–12167

Table 1. Experimental Values of Different Sets of the Synthesis along with TEM and DLS Results

set	SPR (nm)	λ_{CSFE} (nm)	shape (TEM)	DLS results (mid points in peaks)—nm	nucleation stage
I-a	421	264	hexagonal, triangular, truncated, plate-like	few at 5, mostly at 100	15
I-b	425	261	hexagonal, irregular, plate	at 10 = at 100	10
I-c	450	252	rod, irregular, truncated	few at 10 mostly >100	<10
II-a	415	258	irregular, spherical, oval	mostly <10	25
II-b	419	259	spherical, oval	large near 10, some at 45, few up to or >100	20−25
II-c	425	261	oval	mostly b/w 45 and 100. Portion up to 10	20
III-a	439	261	rod	mostly at or >100	15−20
III-b	445	251	hexagonal, triangular, truncated, plate like	portion at 50, mostly at 100	15−20
III-c	455	236	hexagonal, triangular, plate	good portion b/w 5−50, large portion arr. 100	20
IV-a	425	261	spherical	largely up to 100, some>100, few <10	30−35
IV-b	435	249	irregular, plate, rod	good portion up to 10 mostly b/w 50 and 100, few >100	20−25
IV-c	439	244	rod, irregular	good portion < 10, mostly b/w 50 and 100, vs few >100	20
V-a	434	265	irregular	mostly > 00, some up to 100, vs few < 10	10−15
V-b	425	262	oval	a portion <50, large portion b/w 50 and 100, some <10	15
V-c	419	259	spherical	mostly <50, a portion up to 10, few >100	25

However, the increase in the intensity of absorption at λ_{SPR} and the fall of intensity in the absorption of λ_{CSFE} were smooth and more uniform when the [$AgNO_3$] concentration was varied in the presence of SDS.

This indicated an increase in the time period of the nucleation stage in the presence of SDS than in its absence. This led to the explanation that either less seeds were formed or seeds coalesced during the early formative phase in the absence of SDS and hence growth phase started early, leading to large-sized polytope Ag NPs.[52] However, smaller and spherical NPs were formed in the presence of SDS due to seed entrapment and lowering of surface energy.[53] Xia et al. described the possible outcome from thermodynamic perspective by considering the stabilization of seed facets with possible morphology of NPs from a blend of crystal facets, like the ovoid results obtained in the present study.[54] the eqs 1 and 2[55]

$$\gamma = \left(\frac{\partial G}{\partial A}\right)_{n,T,P} \quad (1)$$

where γ, G, and A are the surface energy, Gibbs free energy, and the surface area, respectively. In addition,

$$\gamma = \frac{1}{2} N_b \varepsilon \rho_a \quad (2)$$

where N_b, ε, and ρ indicate the number of bonds to be broken for position restoration, bond strength, and surface atom density, respectively. From the above equations, it can be observed that (γ_{111}) consisted of least surface energy. Considering the lattice constant for Ag as 0.409 nm, the stability would tend to fall in the (γ_{200}), (γ_{220}), and (γ_{111}) fashion.[54] Therefore, the NPs must have been formed in octahedral or tetrahedral shape showing strong affinity for the {111} facet. However, largely, mix facetted NPs (Wulff polyhedrons) are obtained.[56] Although the octahedral shape was obtained in the absence of SDS, the oval shape may have resulted due to the overall decrease in the surface energy of {111}, {200}, and {220} facets of Ag NP seeds during the developing phase by the SDS surfactant[54] (more details are given in Section 3.5 under Structural Analysis).

3.2. Effect of Reagent Concentrations on SPR. When [$AgNO_3$] was varied from 0.1 to 1 mM, the SPR showed a major red shift from 421 to 455 nm in the absence of SDS while a moderate red shift appears from 415 to 425 nm in the presence of SDS (Figure S3). The observation was attributed to the increase in the size of Ag NPs in the same way as in SDS variation and was clearly seen from the transmission electron microscopy (TEM) and DLS images (Figures S4 and S5).

In the absence of SDS in set I, triangular and hexagonal Ag NPs were obtained at 0.1 mM [$AgNO_3$], whereas large hexagonal and rod-shaped NPs were vivid at 1 mM. With the increase in [$AgNO_3$], the UV peak at 350 nm became distinct. It was feebly observable in the case of 0.1 mM, moderately at 0.5 mM, and clearly in 1 mM initial [$AgNO_3$]. These observations were found to correlate smoothly with the occurrence of rod-shaped Ag NPs in the same sequence at those concentrations, as was noticeable from the TEM images (Figure S4.1a−c).[57] Another UV absorption peak was observed at 290 nm as the [$AgNO_3$] was increased from 0.1 to 1 mM. This peak became recognizable at 1 mM concentration, which emulated with the factor of nanorods found quite predominant at 1 mM concentration. Also, an absorption eminence was found at 530 nm in the case of 0.5 mM, where the Ag NPs were mostly of flat hexagonal shape.[57] The uneven higher UV−visible absorption readings in the case of 1 mM could be due to aggregations and commencement of large-sized, irregular Ag NPs.[58]

In the presence of SDS in set II, the UV−visible absorption scans did not show humps in the regions 290 and 350 nm or the minor swell at 525 nm with [$AgNO_3$] variation, which implied spherical Ag NPs as were confirmed in the TEM images (Figure S4.2a−c). The scans did not increase abruptly and as appreciably as in the absence of SDS pointing toward the uniform synthesis process, which manifested in uniform spherical and oval shaped Ag NPs. Also, the UV−visible spectra of all sets while varying [$AgNO_3$] concentration in SDS produced smooth SPR curves at higher time periods and at higher [$AgNO_3$] of 1 mM. This specified the stability of finer uniformly sized Ag NPs at higher [$AgNO_3$], which pointed out the size control of the SDS in the development of Ag NPs.[53] Also, when the [$AgNO_3$] concentration was varied in SDS, the UV−visible spectra of all sets produced smooth SPR curves at higher time periods and at higher [$AgNO_3$] up to 1 mM. This specified the stability of finer uniformly sized Ag NPs at higher [$AgNO_3$], which pointed out the size control of the SDS in the development of Ag NPs.[53]

In set III, keeping the [$AgNO_3$] constant and with increasing [CSFE] in the reaction mixture by 5, 10, and 20% in the

https://doi.org/10.1021/acsomega.1c00847
ACS Omega 2021, 6, 12155−12167

absence of SDS, the SPR of the synthesized Ag NPs exhibited a red shift as reported in Table 1. This could be correlated with the increase in size and the presence of triangular, hexagonal, or rod-shaped Ag NPs in all the three [CSFE] cases here (Figure S4.3a−c). The absorption at 350 nm was not visible in early stages (until 30 min) at lower [CSFE]. However, it became visible at higher [CSFE] of 10 and 20% from the early stages of nucleation (15−20 min) in the UV−visible scans. This could be ascribed to the formation of less seeds and the early initiation of growth phase in the reaction at lower [CSFE].[52] It could also be attributed to selective crystallite facet stabilization of {220} and growth along {111} and {200}, leading to the formation of bar and rod-shaped Ag NPs.[59] As the [CSFE] was increased, the stabilization, hexagonal shape, and apartness of NPs were also found to increase. This could be associated with the enclosing and stabilizing of Ag NPs.[60]

In the constant [SDS] of 11 mM and [$AgNO_3$] of (1 mM), SPR exhibited a red shift from 425 to 439 nm in set IV, where the [CSFE] was varied from 5 to 20% (Figure S3j−l). This could be attributed to the shift in the texture of the Ag NPs in terms of both shape and size, as was observed in the TEM images (Figure S4.4a−c). A consistent shift was observed from spherical and oval through irregular to nanorods as the [CSFE] was increased in the reaction mixture. With the increase in [CSFE], the peak at 290 nm showed feeble increase in intensity in the presence of SDS and was not observed at lower [CSFE]. Also, the absorption peak at 350 nm shifted from being less distinct at lower [CSFE] to well distinguished at higher [CSFE]. This might also be correlated with the observation of hexagonal Ag NPs and nanorods in the samples as the [CSFE] was increased in the reaction mixture. It indicated a kind of an antagonistic relationship between CSFE and SDS in terms of directing Ag NPs toward rod-shaped and polytope morphology, with CSFE having polytope effect while SDS having spherical and oval textural effects. The absorption at 350 nm was not apparent at 5% [CSFE] in the reaction mixture. However, as the [CSFE] was increased to 10 and 20%, it became visible after 60 and 40 min, respectively. This could be attributed to the increased effect of CSFE on the reaction during the synthesis process, which appears here to have worked antagonistically to the surfactant [SDS]. By these observations, it could be opined that CSFE stabilizes the crystal facets {111} and {220} or only one of them while as SDS stabilizes all the facets without any preference leading to oval or spherical Ag NPs.[52,54]

Set V includes [SDS] variation. Here, [$AgNO_3$] and [CSFE] were kept constant in the reaction mixture as 0.5 mM and 10%, respectively, whereas [SDS] was varied as premicellar (4 mM), cmc (8.2 mM), and post cmc (11 mM). The SPR peak value for the synthesized Ag NPs showed a hypsochromic shift in the order of 434, 425, and 419 nm (Figure S3. m−o). With the increase of [SDS] in the reaction mixture, these observations could be ascribed to the successive shift in size to the lower range (58 to 19 nm) and the increase in distribution of the synthesized Ag NPs (Table S2).[61] It was evident from the data of DLS (Figure S5.m−o) and TEM images of the samples synthesized at respective [SDS] (Figure S4.5a−c). No appreciable absorptions were found in UV−visible at 290, 350, and 530 nm at the three respective [SDS]. This observation could also be matched with the TEM images of the three [SDS] cases, where no trigonal, hexagonal, or rod-shaped Ag NPs were found (Figure S4.5). In all the three [SDS] cases, a consistent increase in the UV−visible absorption with time was found, which delineated that the nucleation and growth phases were proceeded with smooth and regular manner.

3.3. Shape, Size, and Dispersion. While varying the [$AgNO_3$] concentration, the synthesized Ag NPs of sets I and II (absence and presence of SDS) exhibited two peaks in the DLS images. The second peak was found to be intense at all concentrations in the case of set I, but its intensity increased with the increase in [$AgNO_3$] in set II (Figure S5a−f). One reflection that matched with this trend was that when [$AgNO_3$] was varied in the absence of SDS, the Ag NPs formed were shaped as hexagonal, triangular, and plate-like. However, similar spherical and oval shaped Ag NPs were formed in the presence of 11 mM-SDS at all [$AgNO_3$]. Only the size got increased with the increase in [$AgNO_3$] in set II.

Also, from Figure S5c,f, it could be observed that Ag NPs showed more aggregation into high sized colloidal particles in the absence of SDS than in its presence. This was apparent from TEM images, which revealed that even at higher [$AgNO_3$] in the presence of SDS, the dispersity remained intact, whereas in the absence of SDS, agglomeration and flocculation occurred leading to coalescence and huge increase in size of Ag NPs (Figures S4.1c and S4.2c).

Varying [CSFE] both in set III and set IV produced an interesting observation. With the increase in [CSFE], the size decreased as the dispersion increased in Ag NPs. This could be attributed to the formation of insufficient nuclei in lower [CSFE] at the nucleation stage. That led to the subsequent deposition of Ag° atoms at the surfaces of those moderate numbers of nuclei, which resulted in large sized rod or plate-like Ag NPs and their insufficient stabilization at lower [CSFE] and smaller polytope Ag NPs with peptization at higher [CSFE] (Figure S8c,d).[62]

Also, in set III, when the [CSFE] concentration was increased at constant [$AgNO_3$], large hexagonal Ag NPs were formed with a good stabilization in the absence of SDS (Figure S4.3c and S5.i). This could be attributed to the presence of enough [CSFE] for reduction, encapsulation, and protection of Ag NPs from agglomeration and sedimentation.[5] However, at higher [CSFE], beyond the cmc of SDS (11 mM) and 1 mM [$AgNO_3$] in set IV, the SDS paced down the synthesis process with the availability of more reducing agent and lesser number of Ag nuclei formed at nucleation stage. It formed a situation of less nuclei and more reduced Ag° atoms, leading to deposition and growth in the already formed nuclei, which instigated the formation of Ag nanorods as were observed in the TEM images of the samples (Figures S4.4c and S5i,l).

Keeping [$AgNO_3$] as 1 mM and [SDS] as 11 mM, the variation of [CSFE] produced results which were antagonistic to SDS results in terms of shape of Ag NPs (Figure S4.4a−c). While the dispersity was predominant at lower [CSFE] (5%), rod shape was predominant in the higher concentration (20%) of CSFE, with dispersity being the SDS effect while rod shapes being the CSFE effect (Figure S5j−l).

In set V, where [SDS] was varied as 4, 8.2, and 11 mM, while keeping the [$AgNO_3$] and [CSFE] constant in the reaction mixture, it was found that Ag NPs shifted uniformly from partly coalesced through partly dispersed to well dispersed in the solution (Figure S5m−o). This was observed from the TEM images (Figure S4.5a−c) and histograms (Figure S7.13-15). The size of Ag NPs showed uniform progression toward the lower range (10 nm) with an increase in dispersity. It was attributed to the encapsulating effect of

https://doi.org/10.1021/acsomega.1c00847
ACS Omega 2021, 6, 12155−12167

SDS, which assisted in the size control and stabilization.[63] When the concentration of SDS was increased beyond the cmc value (11 mM), the influence of SDS becomes more prevalent, and only spherical, oval, and finely dispersed Ag NPs were found.[62] This again could be confirmed from the histogram data which showed a shift from 1.5 to 1.4 in terms of μ_L/μ_B ratio, indicating a shift in tendency from rod-shaped toward spherical Ag NPs (Table S2, set V).

3.4. Kinetics and Stability. *3.4.1. Kinetic Studies.* From the kinetic studies through UV−visible spectrophotometry and conductometry, the nucleation, growth, and aggregation stages were found quite harmonious and resembling with other findings in the synthesis of Ag NPs.

In order to study the varying concentration effect, the process of synthesis was carried between 0.1 and 1 mM of [$AgNO_3$] from 5 to 20% of [CSFE] and the SDS was varied as pre, cmc, and post cmc as 4, 8.2, and 11 mM. The model embraced was of Esumi and the parameters, especially "detected first order" rate constant-K_{dfo}, were derived graphically from $\ln(1 - A_T/A_\alpha)$ versus time (minutes) plots (Figure S6).[41,64] A_T and A_α are the absorbances at T and α time, respectively. Here, the formations of Ag NPs were treated in relation to the usage of reactant Ag^+ ions from $AgNO_3$. As can be seen from Table S3, the rate constant value increased abruptly (4.45 to 8.10 × 10^{-5} s^{-1}) in the absence of SDS, while a modest increase (5.56 to 6.11 × 10^{-5} s^{-1}) was observed in its presence. Again, when the [CSFE] variation was plotted, a similar trend was seen in the absence and presence of SDS (Figure S6b,d). When the SDS was varied while keeping other reagents constant, a fall was seen at cmc (3.36 × 10^{-5} s^{-1}) with more increase toward post cmc side of [SDS]. This thing stayed understood from nucleation and growth stages of Ag NPs from Figure S8 also, where it was clear that SDS increased the time of nucleation stage, which led to increase in the concentration and distribution of formed Ag NPs (Figure S4.5c). The antagonistic relation can also be seen here from the K_{dfo} values; when the [SDS] concentration was increased at constant [CSFE], there was a decrease from 5.44 to 3.36 × 10^{-5} s^{-1} as the concentration becomes comparable, and then it raised again to 5.91 × 10^{-5} s^{-1} as the SDS concentration was increased beyond the cmc value.

From the observed rate constant-K values with respect to CSFE, when the [$AgNO_3$] was increased from 0.1 to 1 mM in the absence of SDS, there was a marginal change in the K_{dfo} values (1.71 to 1.39 × 10^{-2} s^{-1}). However, in the presence of SDS, increased K_{dfo} values from 1.61 to 4.64 × 10^{-2} s^{-1} were observed. At a higher [$AgNO_3$] concentration of 1 mM, in the absence of SDS, when the [CSFE] concentration was increased, the K_{dfo} values showed a regular increase from 1.34 to 4.66 × 10^{-2} s^{-1}, but in the presence of SDS, there was a fall in the K_{dfo} value at higher [CSFE], (4.67 to 1.12 × 10^{-2} s^{-1}), which relates to the antagonistic effect of CSFE, where the effect of CSFE surpassed the control by the SDS, leading to rapidness in the process in the nucleation and early growth phase and hence the rate matched to K_{dfo} in the absence of SDS (Table S4, set IV). This effect was also seen by decreasing the rate constant K_{dfo} values (5.24 to 4.43 × 10^{-2} s^{-1}) when only the [SDS] concentration was increased. As the [SDS] concentration was increased, the K_{dfo} values decreased, which indicated the antagonistic effect of SDS to CSFE's effect on the reaction.

At post cmc [SDS], when the Ag NP synthesis was kinetically studied with respect to [CSFE] with time (Figure S6d,h) and at 20, 25, and 30 °C (Figure S6k,l), the NP formations were found to be well-fitted to first-order kinetics as observed from linearity of graphs, K_{dfo}, and R^2 values (Table 2). An increase in K_{dfo} values was found from 2.95 to 3.64 × 10^{-5} s^{-1} in the absence of SDS while nearly a constant value (6.58 to 6.68 × 10^{-5} s^{-1}) was observed in the presence of SDS. The kinetics of Ag NP synthesis with respect to [CSFE] showed that the correlation factor (R) value ascended in the presence of beyond cmc [SDS] and at different temperatures (Tables S4 and 2), which signified the first-order kinetics concerning CSFE utilization in the synthesis of Ag NPs. This observation was used to derive an autocatalytic mechanism as described in the Supporting Information (Scheme S1).[64]

Table 2. K_{dfo} and R^2 Values for the Synthesis of Ag NPs at 20, 25, and 30°C

T in °C	[$AgNO_3$] 10^{-4} molar	[CSFE] % by volume	[SDS] 10^{-3} molar	K_{dfo} 10^{-5} (s^{-1})	correlation factor—R^2
20	5	5		2.95	0.9097
25	5	5		3.71	0.9301
30	5	5		3.64	0.7733
20	5	5	11	6.58	0.9958
25	5	5	11	6.71	0.9917
30	5	5	11	6.68	0.9735

From Tables S3 and S4, it was clear that the reaction showed change in K_{dfo} with respect to both reactants, $AgNO_3$ and CSFE. However, since the R^2 values in Table S4 fell below 0.9 often, this data could be used more for qualitative inference than quantitative. Table S3 showed linear variation with respect to both $AgNO_3$ and CSFE, but when the same process is studied with respect to [CSFE] (Table S4), it appeared as first-order reaction with respect to [CSFE] only. Therefore, when combining information from discussion, it appeared that the reaction followed pseudo-first-order kinetics with autocatalytic mechanism (Scheme S1, Supporting Information).[35,64]

3.4.2. Stability Studies. The cmc of SDS was found to be 8.2 mM in DD H_2O at 25 °C (Figure S9a). In the nanosolutions prepared in the absence of SDS, it decreased to 6.2 mM (Figure S9b), which indicated a strong positive interaction between the surfactant and the synthesized Ag NPs.[65] An important observation made was that, though the specific conductance increased with increasing [$AgNO_3$] in the reaction mixture, the cmc decreased from 6.2 to 5.9 mM (Figure S9b). This may be due to the size effect of the formed Ag NPs, the SDS-NP interaction, and CSFE-SDS interaction.[66] The decrease in size initiated the increase in the zeta potential, which could be the reason in the increase in the specific conductance of the NP solution (Table 3).[22,67] It has been observed that proteins interact with amphiphiles and also resulted in protein−corona outcome from their interaction with nanoparticles.[68,69] This might have led increased interaction between SDS and Ag NPs due to CSFE.

Also, from the kinetic studies through conductometry, the nucleation, growth, and aggregation stages were observed. It could be seen that the nucleation stage is extended in the presence of SDS than in its absence (Figure S10a,b), which was in accordance with the UV−visible spectrometric findings.

It has been mentioned in the literature that the colloidal solutions with the zeta potential between ±5 flocculate, ±10 to ±30 have nascent to moderate stability, and above ±30 the colloids achieve good stability with every increase in the zeta

https://doi.org/10.1021/acsomega.1c00847
ACS Omega 2021, 6, 12155−12167

Table 3. Average Measured Values of Zeta Potential, Mobility, and Conductivity of the Synthesized Ag NPs[a]

s. no	S-1	S-2	S-3	S-4	S-5	S-6	S-7
zeta potential mV	−16.8	−13.7	−12.3	−14.1	−33.2	−36.1	−34
mobility μm cm/V s	−1.32	−1.075	−0.9644	−1.109	−2.603	−2.828	−2.665
conductivity mS/cm	0.0874	0.163	0.298	0.128	0.616	0.749	0.852

[a][$AgNO_3$] S_1−S_3 and S_5−S_7 = 0.5, 1, and 2 mM; S_4 = 0.5 mM (except S_4, [CSFE] = 5% and S_4 = 10%), ([SDS] S_5−S_7 = 11 mM).

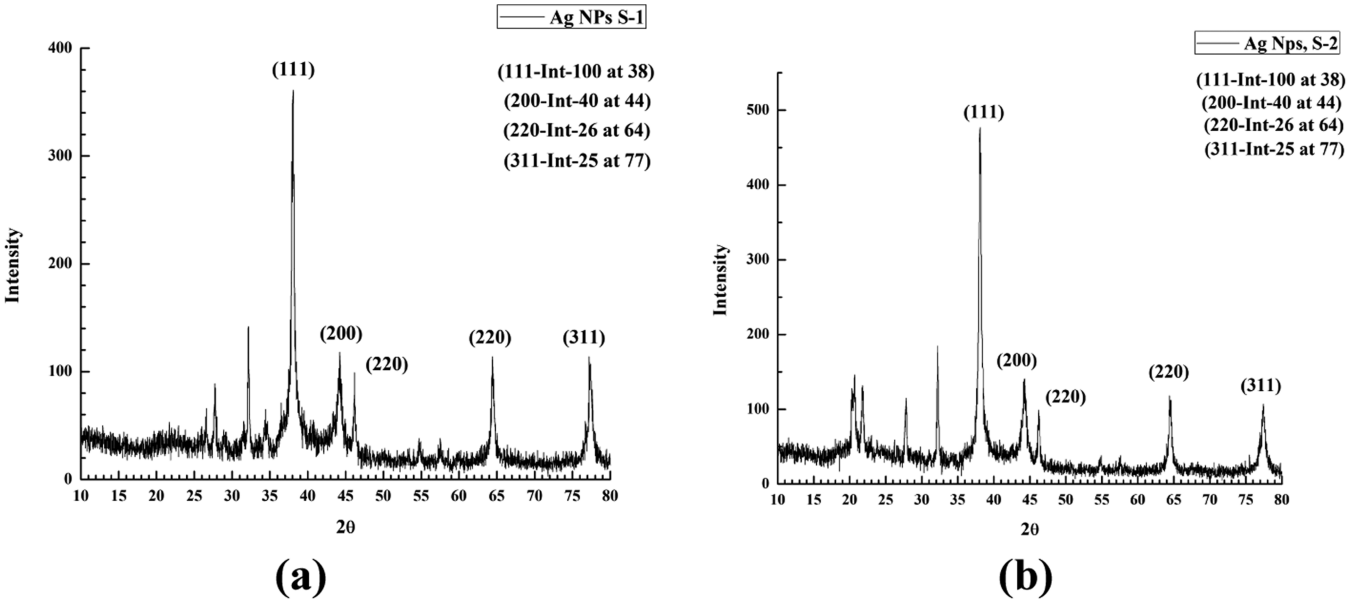

Figure 2. XRD images of Ag NPs synthesized (a) in the absence of SDS and (b) in the presence of SDS.

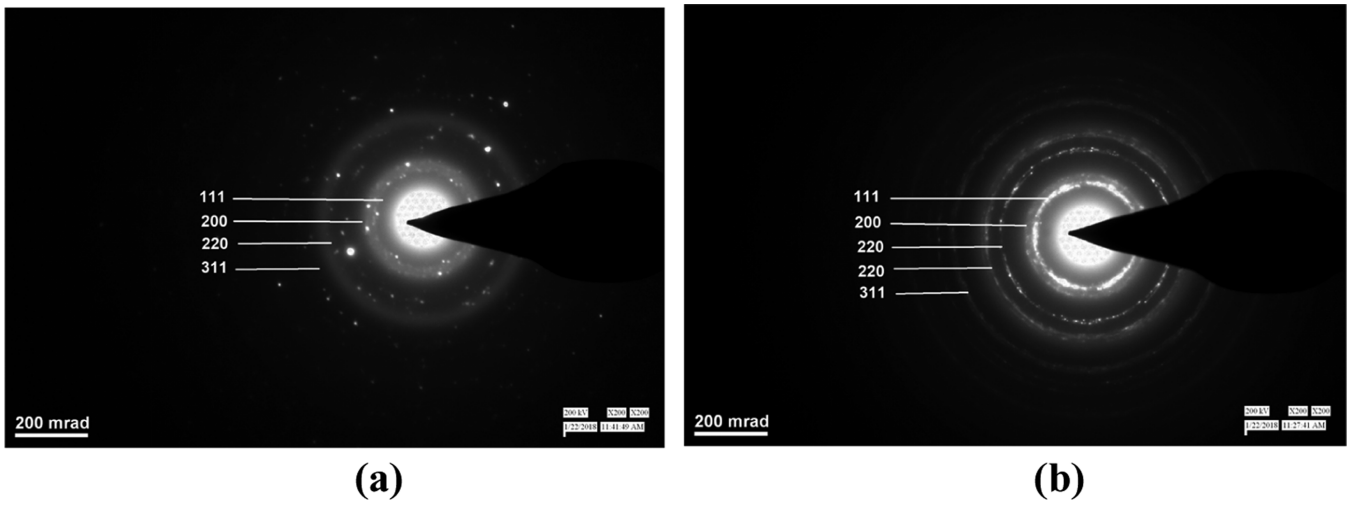

Figure 3. SAED pattern of Ag NPs synthesized (a) in the absence of SDS and (b) in the presence of SDS.

value.[36,70] Table 3 and Figure S11 show that the synthesized Ag NPs in the presence of SDS showed more stability (−33 to −36) than in the absence of SDS (−12 to −16). Also, mild stabilizing ability of CSFE was observed by increase in stability with increase in [CSFE] (Table 3). Overall, in the absence of SDS, the stability decreased with the increase in [$AgNO_3$] while as in the presence, it first increased up to 1 mM [$AgNO_3$] and then decreased (Figure S11).

3.5. Structural Analysis. In order to obtain good yield for XRD analysis, set III.c and set IV.c (Table S1) were chosen. From the data plotting of XRD (Figure 2) and SAED patterns (Figure 3), it was observed that both conditions of absence and presence of SDS produced Ag NPs of polycrystalline nature. In addition to TEM images, the mean size of crystallites of synthesized Ag NPs was also calculated by the Debye−Scherrer equation[71]

$$\text{size, } D = \frac{(0.9 \times \lambda)}{(\text{FWHM} \times \cos\theta)} \quad (3)$$

where λ was the wavelength of X-rays, FWHM was the width at halfway intensity of XRD peak, and cos θ was the angle in radians. The size was determined by measuring the average size from four major peaks from XRD graphic data. The size was found 24.5 nm in the absence of SDS (Figure 2a) and 19 nm in

https://doi.org/10.1021/acsomega.1c00847
ACS Omega 2021, 6, 12155−12167

its presence (Figure 2b). The nanoparticle size obtained microscopically from TEM agreed to XRD data. The most noticeable peaks from the XRD graphs of both synthesized Ag Np samples specified JCPDF no. 040783. The sharp multiple peaks in XRD graphs and the clear ring patterns in TEM−SAED pattern (Figure 3) verified crystalline grains of Ag NPs with the corresponding facets of face-centered cubic (fcc) Ag planes as (111), (200), (220), and (311) in the increasing order of 2θ, with (111) being the most intense peak (Figure 3a,b). As the XRD data revealed the most intense peak being at 38°, Bragg's equation

$$n\lambda = 2d \sin\theta \quad (4)$$

together with $d = a/\sqrt{(h^2 + k^2 + l^2)}$ and $a = 2r\sqrt{2}$ for fcc, the sum value for h, k, and l was found to be 3.12, thus confirming the principal peak as (111) at 38°, while the values of 4.13, 8.28, and 11.42 were calculated for 200, 220, and 311 peaks, respectively.[8] The shape formation during the synthesis of Ag NPs could be described in relation to the CSFE and SDS stabilization and preferential growth of these observed FCC crystal facets while assessing eqs 1 and 2.[26]

3.6. Antifungal Analysis. Owing to the antimicrobial effectiveness of SDS, only set I.b synthesized Ag NPs were analyzed for antimycotic analysis, which were synthesized in the absence of SDS.[72,73] The synthesis concentrations of CSFE and $AgNO_3$ did not exhibit any fungicidal outcome. Ales Panáček et al. have reported the antifungal testing of Ag NPs against *Candida* sp. The synthesis was carried through Tollens method in the presence of SDS, and the nanoparticles were of spherical shape.[73] Xia et at. put forward similar results of MIC for chemically synthesized spherical Ag NPs.[22] Elamawi et al. tested spherical Ag NPs on plant fungal pathogens with 25−91% inhibition rate.[74] However, it has been mentioned in the literature that the antimicrobial activity gets enhanced by chemical reduction methods because of the adsorption of reaction leftover chemicals on the surface of the nanoparticles.[72] Also, the authors reported that the antimicrobial activity depends on the morphology with spherical nanoparticles showing promising antifungal activity. Biologically synthesized nanoparticles show promising antifungal activity with an advantage of being encapsulated and stabilized by organic compounds from plant extracts.[60] Paul et al. described the antimycotic essays against *Candida* sp. at 31−250 μg/mL MIC for C−Ag NPs.[75] In the undertaken study here, as the polytope Ag NPs which had been obtained in absence of SDS were tested for antimycotic activity instead the spherical Ag NPs, it could be the reason why the lowest MIC values were obtained slightly above, 0.3 mM than the reported 0.1 mM by Panáček et al.[73]

Anatomical protein and DNA interaction have been described as the possible mechanism for antimycotic action of Ag NPs. The Ag NPs permeated through fungi cell wall and amassed in cell organelles which rendered them malfunctional and led to cell death.[22]

3.6.1. MIC and MFC. MIC was defined as the minimum amount of the drug/compound required to inhibit the *Candida* growth confirmed by measuring turbidity (OD_{595}), while MFC was defined as the minimum amount of drug that terminated all the cells and at which no colony developed on the solid media after 48 h of incubation. The MIC values of Ag NPs against *C. albicans* (ATCC 90028 and 10261) and *Candida glabrata* (ATCC 90030) were determined as 0.0625 mM for both samples. For *Candida tropicalis*, it was detected as 0.03125. The MFC of Ag NPs against the same strains was found as 0.125 mM. The corresponding MICs and MFCs of Ag NPs against all the strains were listed in Table 4.

Table 4. MIC and MFC Values of Synthesized Ag NPs Against Various *Candida* Strains in the Absence of SDS

s. no.	*Candida* strain	MIC (mM)	MFC (mM)
1	*C. albicans* (ATCC 90028)	0.0625	0.125
2	*C. albicans* (ATCC 10261)	0.0625	0.125
3	*C. tropicalis* (ATCC 750)	0.0312	0.125
4	*C. glabrata* (ATCC 90030)	0.0625	0.125

It was quite clear from the studies that Ag NPs synthesized using *C. siamea* extract showed antifungal activity against all the considered fungal strains. From the MIC and MFC values of Table 4, it was found that the Ag NPs were most effective against *C. tropicalis* (ATCC 750) (Figure 4c) for which the values were 0.0312 and 0.125 mM/L, respectively.[76]

3.6.2. Growth Curve Studies in Candida Species. Growth studies showed the prominent inhibitory effect of Ag NPs on *Candida* cells.[24] The inhibition was visible even at very low concentration. At all sub-MIC values, there was a delay in the exponential phase. The relative growth patterns of *Candida* strains in the presence of Ag NPs were illustrated in Figure 4a−d.

From the growth curve studies, it was evident that synthesized Ag NPs delayed the growth of all reckoned strains of fungi. It was clear from the plotted graphs that the strains showed no growth up to first 2 h of inoculation, very little growth in the next 2 h, and a marginal growth after 6 h of impregnation of *Candida* strains. This observation could be used in the significance of using Ag NPs with another fungicidal medication, by the fact that the efficiency of the medicine could not only be enhanced but also made more effective in less time required for the treatment. Also, Ag NPs could be impregnated into materials to make them microbial repellent and hence an effective remedy for infection prevention.

As depicted in Scheme 2, the effectuated study clued toward contrary relationship between the reducing agents CSFE and SDS in terms of the textural outcome of Ag NPs. As discussed, the dissimilar stabilization of {111}, {200}, and {220} FCC Ag crystallite facets led to rod, polytope, and quasispheroidal Ag NPs.[8,26] The best disparities in the shape were found when the [CSFE] was varied either in the absence or in the presence of SDS. Without SDS, the [CSFE] variation formed rod and polytope Ag NPs and produced quasi-spherical and oval Ag NPs in beyond cmc [SDS]. However, Ag NP formation transformed from spheroidal toward polytope and with emergence of rod shape as the [CSFE] was increased, at above cmc [SDS]. A *Cassia* sp. chromone based autocatalytic mechanism was proposed with the rate of reaction being observed as pseudo-first order with respect to [CSFE] (Scheme S1, Supporting Information).[76]

4. CONCLUSIONS

In the absence of SDS, the Ag NPs were formed with polytope texture in the form of triangular, hexagonal, and rod-shaped nanoparticles, whereas oval and spherical Ag NPs were obtained in the presence of SDS. The increase in [$AgNO_3$] and [CSFE] reagents during the synthesis of polytope Ag NPs produced a red shift in the SPR, while a blue shift was observed

https://doi.org/10.1021/acsomega.1c00847
ACS Omega 2021, 6, 12155−12167

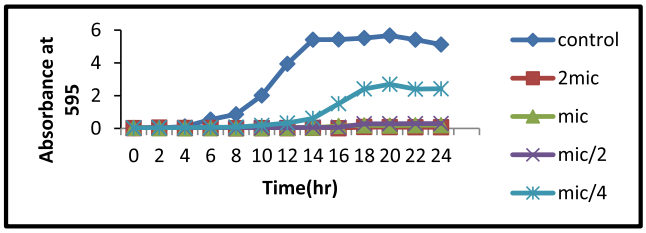

(a)

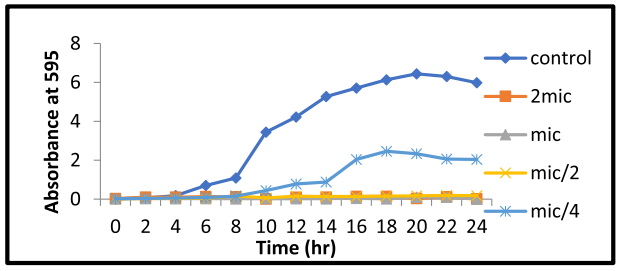

(b)

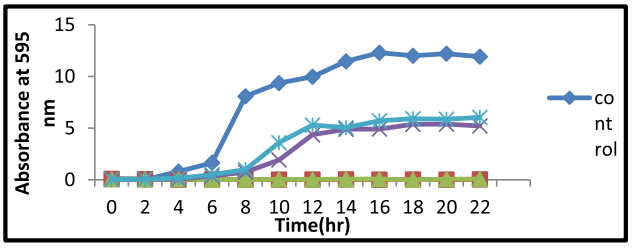

(c)

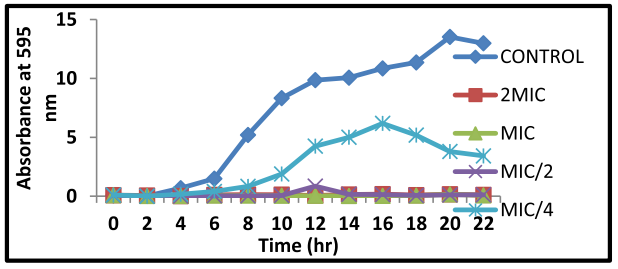

(d)

Figure 4. Growth curve of (a) *C. albicans* (ATCC 90029), (b) *C. albicans* (ATCC 10261), (c) *C. tropicalis* (ATCC 750), and (d) *Candida glabrata* (ATCC 90030) against synthesized Ag NPs.

with the increase in [SDS]. Dispersion was found to decrease with the increase in the size of Ag NPs from DLS data and aggregated colonies of Ag NPs were also visible in the TEM images. The mutual effect of SDS and CSFE was observed with the exhibition of antagonistic textural outcome, which provided an edge to the present study in terms of control over texture and dispersity of biomimetic synthesized Ag NPs. The kinetic data revealed that the SDS increased the nucleation phase and the synthesis followed the pseudo-first-order kinetics. The K_{dfo} values were found to vary smoothly with respect to both Ag NP formation and the with the decrease in [CSFE] as the reaction proceeded. The data from zeta potential indicated that stability increased with the increase in [CSFE] and [SDS], but it decreased with increasing [$AgNO_3$] in the formulation. XRD and SAED data showed that the synthesized Ag NPs were of FCC crystalline nature and with the JCPDF file number of 040783. The antimycotic studies exhibited that all samples of synthesized Ag NPs were active against *Candida* fungal strains and most effective against *C. tropicalis*. Also, from growth curve studies, it was found that Ag polytope NPs inhibited and delayed the growth of *Candida* fungal strains by as much as 6 h. These findings make polytope Ag NPs as viable antifungal agents of future. This current method of synthesis is viable, cheap, and environmentally responsive for the synthesis of polytope and spherical Ag NPs with a control over both texture and dispersity and a good prospect to combat pathogenic fungal infection.

■ ASSOCIATED CONTENT

Supporting Information

The Supporting Information is available free of charge at https://pubs.acs.org/doi/10.1021/acsomega.1c00847.

Mechanism; synthesized Ag NPs; UV−visible spectra; TEM images; DLS images; kinetics; histograms; nucleation, growth, and adsorption; conductivity measurements; zeta potential; Ag NPs synthesis description; histograms values; and (K_{dfo}) and R^2 values (PDF)

■ AUTHOR INFORMATION

Corresponding Author

Abbul Bashar Khan − *Department of Chemistry, Jamia Millia Islamia, New Delhi 110025, India;* orcid.org/0000-0002-9111-1026; Phone: +919456277727; Email: abashar@jmi.ac.in, bashar.khan2009@gmail.com

Scheme 2. Schematic Elucidation of the Synthesis of Ag NPs by CSFE and the Antagonistic Shape Variations

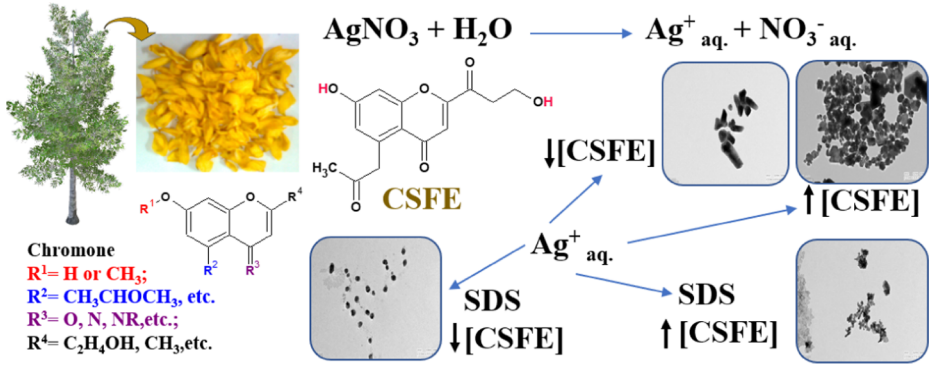

https://doi.org/10.1021/acsomega.1c00847
ACS Omega 2021, 6, 12155−12167

Authors

Sajjad Hussain Parrey − *Department of Chemistry, Jamia Millia Islamia, New Delhi 110025, India*

Mohsin Maseet − *Department of Biosciences, Jamia Millia Islamia, New Delhi 110025, India*

Rabia Ahmad − *Department of Chemistry, Jamia Millia Islamia, New Delhi 110025, India*

Complete contact information is available at: https://pubs.acs.org/10.1021/acsomega.1c00847

Notes

The authors declare no competing financial interest.

■ ACKNOWLEDGMENTS

The authors acknowledge the support from CIF, CRIBSc., JMI New Delhi; SAIF, AIIMS New Delhi; and Horticulture Dept. JMI New Delhi. A.B.K. is thankful to University Grant Commission for UGC-BSR Research Start-Up-Grant (No. F.30-531/2020(BSR)).

■ REFERENCES

(1) Bayda, S.; Adeel, M.; Tuccinardi, T.; Cordani, M.; Rizzolio, F. The History of Nanoscience and Nanotechnology: From Chemical-Physical Applications to Nanomedicine. *Molecules* **2020**, *25*, 112.

(2) Mezgebe, M. M.; Ju, A.; Wei, G.; MacHaria, D. K.; Guang, S.; Xu, H. Structure Based Optical Properties and Catalytic Activities of Hydrothermally Prepared CuS Nanostructures. *Nanotechnology* **2019**, *30*, 105704.

(3) Fariq, A.; Khan, T.; Yasmin, A. Microbial Synthesis of Nanoparticles and Their Potential Applications in Biomedicine. *J. Appl. Biomed.* **2017**, *15*, 241−248.

(4) Akintelu, S. A.; Folorunso, A. S.; Folorunso, F. A.; Oyebamiji, A. K. Green Synthesis of Copper Oxide Nanoparticles for Biomedical Application and Environmental Remediation. *Heliyon* **2020**, *6*, No. e04508.

(5) Aisida, S. O.; Ugwu, K.; Akpa, P. A.; Nwanya, A. C.; Ejikeme, P. M.; Botha, S.; Ahmad, I.; Maaza, M.; Ezema, F. I. Biogenic Synthesis and Antibacterial Activity of Controlled Silver Nanoparticles Using an Extract of Gongronema Latifolium. *Mater. Chem. Phys.* **2019**, *237*, 121859.

(6) Khan, M.; Shaik, M. R.; Adil, S. F.; Khan, S. T.; Al-Warthan, A.; Siddiqui, M. R. H.; Tahir, M. N.; Tremel, W. Plant Extracts as Green Reductants for the Synthesis of Silver Nanoparticles: Lessons from Chemical Synthesis. *Dalton Trans.* **2018**, *47*, 11988−12010.

(7) Fernando, I.; Zhou, Y. Impact of PH on the Stability, Dissolution and Aggregation Kinetics of Silver Nanoparticles. *Chemosphere* **2019**, *216*, 297−305.

(8) Ugwoke, E.; Aisida, S. O.; Mirbahar, A. A.; Arshad, M.; Ahmad, I.; Zhao, T.-k.; Ezema, F. I. Concentration Induced Properties of Silver Nanoparticles and Their Antibacterial Study. *Surf. Interfaces* **2020**, *18*, 100419.

(9) Gilroy, K. D.; Yang, X.; Xie, S.; Zhao, M.; Qin, D.; Xia, Y. Shape-Controlled Synthesis of Colloidal Metal Nanocrystals by Replicating the Surface Atomic Structure on the Seed. *Adv. Mater.* **2018**, *30*, 1−25.

(10) Aisida, S. O.; Ugwu, K.; Akpa, P. A.; Nwanya, A. C.; Ejikeme, P. M.; Botha, S.; Ahmad, I.; Ezema, F. I. Morphological, Optical and Antibacterial Study of Green Synthesized Silver Nanoparticles via Vernonia Amygdalina. *Mater. Today: Proc.* **2019**, *36*, 199−203.

(11) Mohammed, A.; Liman, M. L.; Atiku, M. K. Chemical Composition of the Methanolic Leaf and Stem Bark Extracts of Senna Siamea Lam. *J. Pharmacogn. Phyther.* **2013**, *5*, 98−100.

(12) Nsonde Ntandou, G. F.; Banzouzi, J. T.; Mbatchi, B.; Elion-Itou, R. D. G.; Etou-Ossibi, A. W.; Ramos, S.; Benoit-Vical, F.; Abena, A. A.; Ouamba, J. M. Analgesic and Anti-Inflammatory Effects of Cassia Siamea Lam. Stem Bark Extracts. *J. Ethnopharmacol.* **2010**, *127*, 108−111.

(13) Kamagaté, M.; Koffi, C. Ethnobotany, Phytochemistry, Pharmacology and Toxicology Profiles of Cassia Siamea Lam. *J. Phytopharm.* **2014**, *3*, 57−76.

(14) Thanh, N. T. K.; Maclean, N.; Mahiddine, S. Mechanisms of Nucleation and Growth of Nanoparticles in Solution. *Chem. Rev.* **2014**, *114*, 7610−7630.

(15) Glasscott, M. W.; Dick, J. E. Fine-Tuning Porosity and Time-Resolved Observation of the Nucleation and Growth of Single Platinum Nanoparticles. *ACS Nano* **2019**, *13*, 4572−4581.

(16) Jana, N. R.; Gearheart, L.; Murphy, C. J. Evidence for Seed-Mediated Nucleation in the Chemical Reduction of Gold Salts to Gold Nanoparticles. *Chem. Mater.* **2001**, *13*, 2313−2322.

(17) Henglein, A. Colloidal silver nanoparticles: photochemical preparation and interaction with O2, CCl4, and some metal ions. *Chem. Mater.* **1998**, *10*, 444−450.

(18) Hamouda, R. A.; Abd El-Mongy, M.; Eid, K. F. Comparative Study between Two Red Algae for Biosynthesis Silver Nanoparticles Capping by SDS: Insights of Characterization and Antibacterial Activity. *Microb. Pathog.* **2019**, *129*, 224−232.

(19) Naderi, O.; Nyman, M.; Amiri, M.; Sadeghi, R. Synthesis and Characterization of Silver Nanoparticles in Aqueous Solutions of Surface Active Imidazolium-Based Ionic Liquids and Traditional Surfactants SDS and DTAB. *J. Mol. Liq.* **2019**, *273*, 645−652.

(20) Aisida, S. O.; Ugwoke, E.; Uwais, A.; Iroegbu, C.; Botha, S.; Ahmad, I.; Maaza, M.; Ezema, F. I. Incubation period induced biogenic synthesis of PEG enhanced Moringa oleifera silver nanocapsules and its antibacterial activity. *J. Polym. Res.* **2019**, *26*, 225.

(21) Adebayo-Tayo, B.; Salaam, A.; Ajibade, A. Green Synthesis of Silver Nanoparticle Using Oscillatoria Sp. Extract, Its Antibacterial, Antibiofilm Potential and Cytotoxicity Activity. *Heliyon* **2019**, *5*, No. e02502.

(22) Xia, Z.-K.; Ma, Q.-H.; Li, S.-Y.; Zhang, D.-Q.; Cong, L.; Tian, Y.-L.; Yang, R.-Y. The Antifungal Effect of Silver Nanoparticles on Trichosporon Asahii. *J. Microbiol., Immunol. Infect.* **2016**, *49*, 182−188.

(23) Aisida, S. O.; Ugwu, K.; Akpa, P. A.; Nwanya, A. C.; Nwankwo, U.; Botha, S. S.; Ejikeme, P. M.; Ahmad, I.; Maaza, M.; Ezema, F. I. Biosynthesis of Silver Nanoparticles Using Bitter Leave (Veronica Amygdalina) for Antibacterial Activities. *Surf. Interfaces* **2019**, *17*, 100359.

(24) Rodríguez-Torres, M. D. P.; Acosta-Torres, L. S.; Díaz-Torres, L. A.; Hernández Padrón, G.; García-Contreras, R.; Millán-Chiu, B. E. Artemisia Absinthium-Based Silver Nanoparticles Antifungal Evaluation against Three Candida Species. *Mater. Res. Express* **2019**, *6*, 085408.

(25) Prabhu, S.; Poulose, E. K. Silver Nanoparticles: Mechanism of Antimicrobial. *Int. Nano Lett.* **2012**, *2*, 32−41.

(26) Raza, M. A.; Kanwal, Z.; Rauf, A.; Sabri, A. N.; Riaz, S.; Naseem, S. Size- and Shape-Dependent Antibacterial Studies of Silver Nanoparticles Synthesized by Wet Chemical Routes. *Nanomaterials* **2016**, *6*, 74.

(27) Gharibshahi, L.; Saion, E.; Gharibshahi, E.; Shaari, A.; Matori, K. Structural and Optical Properties of Ag Nanoparticles Synthesized by Thermal Treatment Method. *Materials* **2017**, *10*, 402.

(28) Horikoshi, S.; Serpone, N. Introduction to Nanoparticles. *Microwaves in Nanoparticle Synthesis*; John Wiley & Sons, Ltd., 2013; pp 1−24.

(29) Nilavukkarasi, M.; Vijayakumar, S.; Prathip Kumar, S. Biological Synthesis and Characterization of Silver Nanoparticles with Capparis Zeylanica L. Leaf Extract for Potent Antimicrobial and Anti Proliferation Efficiency. *Mater. Sci. Energy Technol.* **2020**, *3*, 371−376.

(30) Bui, V. K. H.; Park, D.; Lee, Y. C. Chitosan Combined with ZnO, TiO_2 and Ag Nanoparticles for Antimicrobialwound Healing Applications: A Mini Review of the Research Trends. *Polymers* **2017**, *9*, 21.

(31) Jain, S.; Mehata, M. S. Medicinal Plant Leaf Extract and Pure Flavonoid Mediated Green Synthesis of Silver Nanoparticles and Their Enhanced Antibacterial Property. *Sci. Rep.* **2017**, *7*, 15867.
(32) Rafique, M.; Sadaf, I.; Rafique, M. S.; Tahir, M. B. A Review on Green Synthesis of Silver Nanoparticles and Their Applications. *Artif. Cells, Nanomed., Biotechnol.* **2017**, *45*, 1272−1291.
(33) Pisárčik, M.; Jampílek, J.; Lukáč, M.; Horáková, R.; Devínsky, F.; Bukovský, M.; Kalina, M.; Tkacz, J.; Opravil, T. Silver Nanoparticles Stabilised by Cationic Gemini Surfactants with Variable Spacer Length. *Molecules* **2017**, *22*, 1794.
(34) Khan, M. N.; Bashir, O.; Khan, T. A.; AL-Thabaiti, S. A.; Khan, Z. CTAB Capped Synthesis of Bio-Conjugated Silver Nanoparticles and Their Enhanced Catalytic Activities. *J. Mol. Liq.* **2018**, *258*, 133−141.
(35) Zaheer, Z.; Aazam, E. S.; Kosa, S. A. Effects of Cationic and Anionic Micelles on the Morphology of Biogenic Silver Nanoparticles, and Their Catalytic Activity for Congo Red. *J. Mol. Liq.* **2016**, *220*, 364−369.
(36) Khan, M. N.; Khan, T. A.; Khan, Z.; AL-Thabaiti, S. A. Green Synthesis of Biogenic Silver Nanomaterials Using Raphanus Sativus Extract, Effects of Stabilizers on the Morphology, and Their Antimicrobial Activities. *Bioprocess Biosyst. Eng.* **2015**, *38*, 2397.
(37) Han, Y.; Yang, J.; Jung, M.; Han, S.; Kim, S.; Jeon, H.-S. Controlling the Pore Size and Connectivity of Alumina-Particle-Stabilized Foams Using Sodium Dodecyl Sulfate: Role of Surfactant Concentration. *Langmuir* **2020**, *36*, 10331−10340.
(38) Nayan, V.; Onteru, S. K.; Singh, D. Mangifera indica flower extract mediated biogenic green gold nanoparticles: Efficient nanocatalyst for reduction of 4-nitrophenol. *Environ. Prog. Sustainable Energy* **2018**, *37*, 283−294.
(39) Archer, J.; Kolwas, M.; Woźniak, M.; Jakubczyk, D.; Kolwas, K.; Derkachov, G.; Wojciechowski, T. Sodium Dodecyl Sulfate Micro-aggregates with Diversely Developed Surfaces: Formation from Free Microdroplets of Colloidal Suspension. *Eur. Phys. J. Plus* **2019**, *134*, 39.
(40) Que, W.; Jiang, L.; Wang, C.; Liu, Y.; Zeng, Z.; Wang, X.; Ning, Q.; Liu, S.; Zhang, P.; Liu, S. Influence of Sodium Dodecyl Sulfate Coating on Adsorption of Methylene Blue by Biochar from Aqueous Solution. *J. Environ. Sci.* **2018**, *70*, 166−174.
(41) Esumi, K.; Hosoya, T.; Suzuki, A.; Torigoe, K. Formation of Gold and Silver Nanoparticles in Aqueous Solution of Sugar-Persubstituted Poly(amidoamine) Dendrimers. *J. Colloid Interface Sci.* **2000**, *226*, 346−352.
(42) Costa, J. F.; Siqueira, W. L.; Loguercio, A. D.; Reis, A.; Oliveira, E. d.; Alves, C. M. C.; Bauer, J. R. d. O.; Grande, R. H. M. Characterization of Aqueous Silver Nitrate Solutions for Leakage Tests. *J. Appl. Oral Sci.* **2011**, *19*, 254−259.
(43) Bahr, M. N.; Modi, D.; Patel, S.; Campbell, G.; Stockdale, G. Understanding the role of sodium lauryl sulfate on the biorelevant solubility of a combination of poorly water-soluble drugs using high throughput experimentation and mechanistic absorption modeling. *J. Pharm. Pharm. Sci.* **2019**, *22*, 221−246.
(44) Al-Thabaiti, S. A.; Aazam, E. S.; Khan, Z.; Bashir, O. Aggregation of Congo Red with Surfactants and Ag-Nanoparticles in an Aqueous Solution. *Spectrochim. Acta, Part A* **2016**, *156*, 28−35.
(45) Tondre, C.; Hebrant, M. Micellar and Microemulsion Systems to Perform Heterogeneous Reactions, Biphasic Extraction and Solute Transport. *J. Mol. Liq.* **1997**, *72*, 279−294.
(46) Maruno, S. Surface Plasmon Spectroscopy of Thin Composite Films of Au Nanoparticles and PEDOT:PSS Conjugated Polymer. *Org. Electron.* **2019**, *64*, 154−157.
(47) Ider, M.; Abderrafi, K.; Eddahbi, A.; Ouaskit, S.; Kassiba, A. Silver Metallic Nanoparticles with Surface Plasmon Resonance: Synthesis and Characterizations. *J. Cluster Sci.* **2017**, *28*, 1051−1069.
(48) Priyanka, S.; Inala, M. S. R.; Nandini, H.; Kutty, A.; Kiranmayee, P. A Pilot Study on Sun Protection Factor of Plant Extracts: An Observational Study. *Asian J. Pharm. Clin. Res.* **2018**, *11*, 326−329.
(49) Ajayi, E.; Afolayan, A. Green Synthesis, Characterization and Biological Activities of Silver Nanoparticles from Alkalinized Cymbopogon Citratus Stapf. *Adv. Nat. Sci.: Nanosci. Nanotechnol.* **2017**, *8*, 015017.
(50) Tripathi, A. K.; Paliwal, M. K.; Singh, J. Chemical Constituents of Cassia Siamea. *Fitoterapia* **1992**, *63*, 556.
(51) Hu, Q.-F.; Zhou, B.; Gao, X.-M.; Yang, L.-Y.; Shu, L.-D.; Shen, Y.; Li, G.-P.; Che, C.-T.; Yang, G.-Y. Antiviral Chromones from the Stem of Cassia Siamea. *J. Nat. Prod.* **2012**, *75*, 1909−1914.
(52) Wang, Y.; He, J.; Liu, C.; Chong, W. H.; Chen, H. Thermodynamics versus Kinetics in Nanosynthesis. *Angew. Chem., Int. Ed.* **2015**, *54*, 2022−2051.
(53) Li, J.; Diao, X.; Xiao, Y.; Qin, L.; Lin, H.; Li, Q.; Liao, B. Effect of Surfactant SDS on the Morphology and Photocatalytic Performance of Zn_2GeO_4nanorods. *Mater. Res. Express* **2020**, *7*, 085005.
(54) Xia, Y.; Xiong, Y.; Lim, B.; Skrabalak, S. E. Shape-controlled synthesis of metal nanocrystals: simple chemistry meets complex physics? *Angew. Chem., Int. Ed.* **2009**, *48*, 60−103.
(55) Zhang, J.-M.; Huang, Y.-H.; Wu, X.-J.; Xu, K.-W. Energy Calculation for Symmetrical Tilt Grain Boundaries in Iron. *Appl. Surf. Sci.* **2006**, *252*, 4936−4942.
(56) Marks, L. D. Experimental Studies of Small Particle Structures. *Rep. Prog. Phys.* **1994**, *57*, 603−649.
(57) Wang, X.; Chen, S.; Reggiano, G.; Thota, S.; Wang, Y.; Kerns, P.; Suib, S. L.; Zhao, J. Au-Cu-M (M = Pt, Pd, Ag) Nanorods with Enhanced Catalytic Efficiency by Galvanic Replacement Reaction. *Chem. Commun.* **2019**, *55*, 1249−1252.
(58) Lodeiro, P.; Achterberg, E. P.; Pampín, J.; Affatati, A.; El-Shahawi, M. S. Silver Nanoparticles Coated with Natural Polysaccharides as Models to Study AgNP Aggregation Kinetics Using UV-Visible Spectrophotometry upon Discharge in Complex Environments. *Sci. Total Environ.* **2016**, *539*, 7−16.
(59) Wang, Z. L. Transmission Electron Microscopy of Shape-Controlled Nanocrystals and Their Assemblies. *J. Phys. Chem. B* **2000**, *104*, 1153−1175.
(60) Aisida, S. O.; Akpa, P. A.; Ahmad, I.; Zhao, T.-k.; Maaza, M.; Ezema, F. I. Bio-Inspired Encapsulation and Functionalization of Iron Oxide Nanoparticles for Biomedical Applications. *Eur. Polym. J.* **2020**, *122*, 109371.
(61) Hanuš, J.; Libenská, H.; Khalakhan, I.; Kuzminova, A.; Kylián, O.; Biederman, H. Localized Surface Plasmon Resonance Tuning via Nanostructured Gradient Ag Surfaces. *Mater. Lett.* **2017**, *192*, 119−122.
(62) Madubuonu, N.; Aisida, S. O.; Ali, A.; Ahmad, I.; Zhao, T.-k.; Botha, S.; Maaza, M.; Ezema, F. I. Biosynthesis of Iron Oxide Nanoparticles via a Composite of Psidium Guavaja-Moringa Oleifera and Their Antibacterial and Photocatalytic Study. *J. Photochem. Photobiol., B* **2019**, *199*, 111601.
(63) Araujo, L.; Löbenberg, R.; Kreuter, J. Influence of the Surfactant Concentration on the Body Distribution of Nanoparticles. *J. Drug Targeting* **1999**, *6*, 373−385.
(64) Khan, Z.; Al-Nowaiser, F. M. Effect of Poly(Vinyl Alcohol) on the Size, Shape, and Rate of Silver Nanoparticles Formation. *J. Dispersion Sci. Technol.* **2011**, *32*, 1655−1660.
(65) Bakshi, M. S. Micelle Formation by Sodium Dodecyl Sulfate in Water-Additive Systems. *Bull. Chem. Soc. Jpn.* **1996**, *69*, 2723−2729.
(66) Hao, L.-S.; Jia, Y.-F.; Liu, Q.; Wang, Y.; Xu, G.-Y.; Nan, Y.-Q. Influences of Molecular Structure of the Cationic Surfactant, Additives and Medium on the Micellization of Cationic/Anionic Surfactant Mixed Systems. *Colloids Surf., A* **2016**, *511*, 91−104.
(67) Wan, L. S. C.; Poon, P. K. C. Effect of Salts on the Surface/Interfacial Tension and Critical Micelle Concentration of Surfactants. *J. Pharm. Sci.* **1969**, *58*, 1562−1567.
(68) Park, S. J. Protein-Nanoparticle Interaction: Corona Formation and Conformational Changes in Proteins on Nanoparticles. *Int. J. Nanomed.* **2020**, *15*, 5783−5802.
(69) Wu, D.; Xu, G.; Sun, Y.; Zhang, H.; Mao, H.; Feng, Y. Interaction between Proteins and Cationic Gemini Surfactant. *Biomacromolecules* **2007**, *8*, 708−712.

https://doi.org/10.1021/acsomega.1c00847
ACS Omega 2021, 6, 12155−12167

(70) Kumar, A.; Hodnett, B. K.; Hudson, S.; Davern, P. Modification of the zeta potential of montmorillonite to achieve high active pharmaceutical ingredient nanoparticle loading and stabilization with optimum dissolution properties. *Colloids Surf., B* **2020**, *193*, 111120.
(71) Aisida, S. O.; Madubuonu, N.; Alnasir, M. H.; Ahmad, I.; Botha, S.; Maaza, M.; Ezema, F. I. Biogenic Synthesis of Iron Oxide Nanorods Using Moringa Oleifera Leaf Extract for Antibacterial Applications. *Appl. Nanosci.* **2020**, *10*, 305−315.
(72) Kvítek, L.; Panáček, A.; Soukupová, J.; Kolář, M.; Večeřová, R.; Prucek, R.; Holecová, M.; Zbořil, R. Effect of Surfactants and Polymers on Stability and Antibacterial Activity of Silver Nanoparticles (NPs). *J. Phys. Chem. C* **2008**, *112*, 5825−5834.
(73) Panáček, A.; Kolář, M.; Večeřová, R.; Prucek, R.; Soukupová, J.; Kryštof, V.; Hamal, P.; Zbořil, R.; Kvítek, L. Antifungal Activity of Silver Nanoparticles against Candida Spp. *Biomaterials* **2009**, *30*, 6333−6340.
(74) Elamawi, R. M.; Al-Harbi, R. E.; Hendi, A. A. Biosynthesis and Characterization of Silver Nanoparticles Using Trichoderma Longibrachiatum and Their Effect on Phytopathogenic Fungi. *Egypt. J. Biol. Pest Control* **2018**, *28*, 28.
(75) Paul, S.; Mohanram, K.; Kannan, I. Antifungal Activity of Curcumin-Silver Nanoparticles against Fluconazole-Resistant Clinical Isolates of Candida Species. *AYU (An Int. Q. J. Res. Ayurveda)* **2018**, *39*, 182.
(76) Morita, H.; Oshimi, S.; Hirasawa, Y.; Koyama, K.; Honda, T.; Ekasari, W.; Indrayanto, G.; Zaini, N. C. Cassiarins A and B, Novel Antiplasmodial Alkaloids from Cassia Siamea. *Org. Lett.* **2007**, *9*, 3691−3693.

https://doi.org/10.1021/acsomega.1c00847
ACS Omega 2021, 6, 12155−12167